IOP Conf. Series: Earth and Environmental Science **163** (2018) 012054 doi:10.1088/1755-1315/163/1/012054

Internal flow and loss mechanisms of specific speed 160 m-kW shroudless hydro turbine

Z H Liu [1], M Shinji [1], and K Miyagawa [2]

[1] Department of Applied Mechanics, Waseda University, Tokyo, 1690072, Japan
[2] Department of Applied Mechanics and Aerospace Engineering, Waseda University, Tokyo, 1690072, Japan

lzhlegend0106@fuji.waseda.jp

Abstract. High efficiency and low-cost hydro turbines are becoming more popular for medium and small-scale hydropower generation in underdeveloped locations. Because of this, a shroudless hydro turbine of medium specific speed 160 [m-kW] was developed based on a low specific speed 80 [m-kW] design concept previously studied in the author's laboratory. We are aiming to develop an optimal design method and further improve performances of the medium-specific speed 160 [m-kW] shroudless hydro turbine. The most important factors are the internal flow and the loss mechanism of each flow path component. In this study, the internal flow and loss mechanisms were investigated and clarified by experimental and computational approaches. The main loss mechanisms in the double circular cascade is the high swirling strength vortices extending from the guide vane inlet to the outlet near the end wall of guide vanes. Furthermore, it has been found that the interference of the secondary flow and leakage flow, and the tip leakage vortex are the predominant loss mechanisms of the shroudless runner.

1. Introduction

Hydroelectric power is a clean energy with high energy density, and can generate electric power reliably and continuously. However, traditional hydropower plants require the construction of a huge dam which necessitates a significant economic investment and causes environmental damage by submergence upstream from the dam. Thus, attention was recently focused on small- and medium-sized hydropower generation, which do not necessitate such large dams, or economical investments, and generates electricity using the natural flow of rivers.

In hydropower plants, the commonly used Francis turbine is mostly manufactured by casting. However, for small- and medium-sized hydropower stations, runners manufactured by casting cost more than cutting. Therefore, Nakamura et al. [1] proposed a new concept, the shroudless turbine, a highly efficient hydraulic turbine which is less expensive, because runners can be manufactured from a single block of metal by cutting. In addition, the internal flow of Guide Vanes (GV) and Stay Vanes (SV) was clarified by investigating the pressure distribution between GV. The vortex generated at the leading edge (LE) of GV was thought as the main loss mechanism in GV [1, 2]. The flow field in the Runner Vanes (RV) was also investigated the operating point at which the cavitation was occurring. The tip vortex cavitation observed near the Trailing Edge (TE) was thought as the main loss mechanism in RV [2]. Further, the flow angle distribution and total pressure in the Draft Tube (DT) near the outlet of RV were measured by a three-hole pitot tube. Results showed that the DT loss was minimal at the design point [1, 2]. Our final purpose is to develop an optimal design method and further

Content from this work may be used under the terms of the Creative Commons Attribution 3.0 licence. Any further distribution of this work must maintain attribution to the author(s) and the title of the work, journal citation and DOI.
Published under licence by IOP Publishing Ltd

improve the performances. Therefore, more details about loss mechanisms of the double circular cascade and the shroudless runner are needed, especially at the design point.

The performance of the turbine was measured using a model hydro turbine test rig. The end wall static pressure on the shroud side was measured to investigate the pressure field of the double circular cascade and shroudless runner. Moreover, the total pressure and flow angle distribution was measured in DT. The velocity distribution of DT was also calculated from the results above. In addition, Reynolds-Averaged Navier-Stokes equation (RANS) simulations were performed to investigate the steady flow field inside the cascade and the shroudless runner. The loss mechanisms were clarified by comparing experimental and computational results.

2. Experimental Setup

The overview of the test apparatus used in the experiment is shown in figure 1. The water was dropped from the overflow tank 20[m] above ground to power the hydraulic turbine. The water went from the model turbine through the downstream vacuum tank and was discharged to the underground water tank along the downstream piping completing the circuit. In addition, the operating point of the test rig was controlled by an electronic dynamometer directly connected to the model turbine and guide vanes capable of adjusting the opening degree. The electronic dynamometer can change the unit speed N_{11} by adjusting the torque acting on the shaft of turbine. The guide vanes can change the unit discharge Q_{11}. N_{11} and Q_{11} are defined as

$$N_{11} = ND_1He^{-0.5} \tag{1}$$

$$Q_{11} = QD_1^{-2}He^{-0.5} \tag{2}$$

Where N, D_1, He, Q are the rotational speed, runner inlet diameter of hub side, effective head and discharge of the model turbine. The specifications of the model turbine are shown in figure 2. The clearance of the shroud side of RV is 0.3[mm]. The position of the measurement points of end wall static pressure in SV GV and RV are indicated in red. In addition, detailed parameters are shown in table 1.

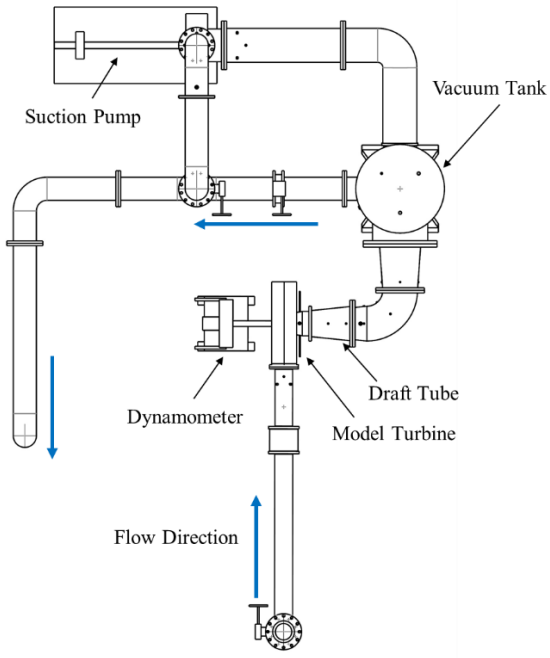

Figure 1. Overview of the test apparatus

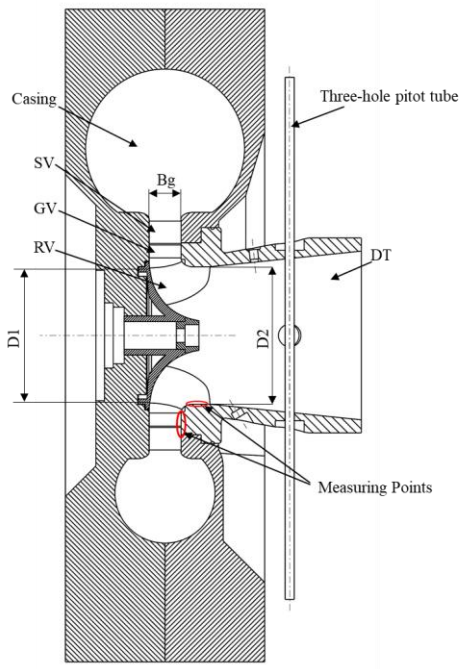

Figure 2. Specifications of the model turbine (cross section)

Table 1. Detailed parameters of model turbine

Items	Values	Units
Specific speed Ns	161.7	m-kW
Effective head He	14.68	m
Design point flow rate Q	0.07255	m^3/s
Design point rotation speed N	1500	rpm
Power P	9.6	kW
Casing type	Spiral	-
Number of stay vanes Zs	20	-
Number of guide vanes Zg	20	-
Number of runner vanes Zr	18	-
D1	0.1578	m
D2	0.1579	m
Bg	0.0380	m

In the table 1, the specific speed was defined as

$$Ns = NP^{0.5}He^{-1.25} \quad (3)$$

When performing the efficiency test, the guide vane opening was adjusted from 110% in increments of 10% to 30%. The rotation speed coefficient N_{11} was adjusted from 72 to 52 in increments of 5 with respect to each GV opening. Specifically, the flow rate in the test apparatus was measured using an electromagnetic flowmeter. A differential pressure transducer was used to measure the static pressure difference between the inlet of the casing and the outlet of the draft tube. In addition, the rotational speed of the turbine was measured using a non-contact type tachometer, and the torque on the axis of the turbine was measured with an electric dynamometer. All the measured data was collected by the data collection device (DAQ) and incorporated into the system development software LabVIEW.

During internal flow measurements, a multipoint pressure sensor device (DSA3207) was used to obtain the static pressure at the end wall of cascades and RV shroud side. It was also used to collect the total pressure data of the pitot tube. The data was measured every 250 microseconds and averaged after collecting 200 samples. It was discharged with the averaged value as one frame and we collected 100 frames for one measurement.

3. Computational Framework

Integral flow computation was performed using a general-purpose code called ANSYS CFX 17.2. Steady state computation using the Reynolds-Averaged Navier-Stokes equation (RANS) was performed with the SST k-ω (Shear Stress Transport) turbulence model to understand the steady performance and internal flow of the turbine. The SST k-ω turbulence model is suitable and practical for the numerical analyses of turbine or pump flow [3-6]. It is effective to estimate the separation flow near the surface of blades. Figure 3 shows the analysis domains: the casing, SV, GV, RV and DT. ICEM CFD 17.2 was used for the casing and DT, Turbo Grid 17.2 for SV, GV and RV. The meshes of all analysis domains are hexahedral. Table 2 shows the detailed mesh information, and figure 4 presents a detailed view of the mesh lines in cascades and DT. The Mixing-Plane model was used for the interface between GV and RV, and the Frozen Rotor model between RV and DT to model frame and pitch change. Additionally, the General Grid Interface (GGI) [7] is applied on all domain interfaces that the topology of meshes at both sides of interfaces does not have to match with each other.

Experimental results at the inlet were used as a boundary conditions and an average static pressure 0 [Pa] was applied at the outlet of the DT. The rotational speed of RV was also set to the values from the experimental results.

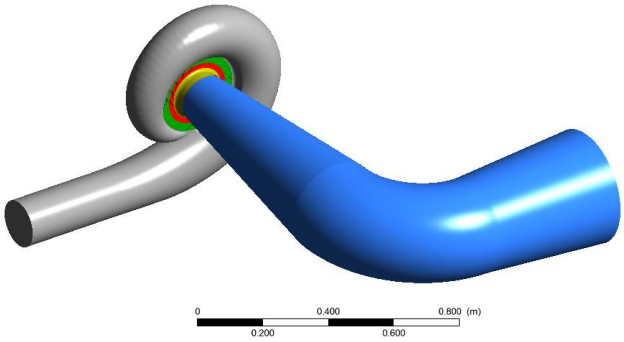

Figure 3. View of analysis domains

Table 2. Detailed mesh information

Flow domains	No. of nodes	Mean y^+
Casing	3740624	17
SV	4009620	1.5
GV	4274200	3.8
RV	14839470	1.1
DT	2265076	19
Total	29128990	

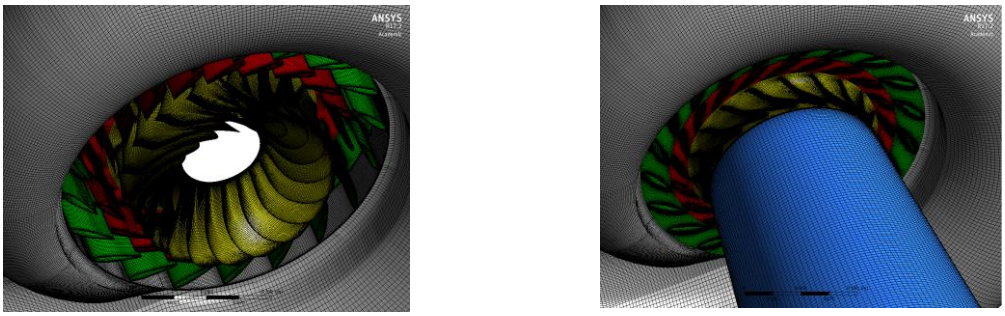

Figure 4. Mesh lines in cascades (left) and DT (right)

4. Turbine Efficiency and Loss Distribution

Figure 5 shows the experimental and computational results about the efficiency of the model turbine at Q_{11} of each operating point. In this figure, Q_{11} is normalized by $Q_{11}{}_{\text{B.E.P.}}$ (Best Efficiency Point). Both results are in qualitative agreement with each other around the design point. Thus, the performance prediction accuracy of the model turbine by computation is confirmed. The experimental results are overall lower than computational results because the disc friction and the leakage loss are ignored in computations. Furthermore, results on the low discharge points show larger deviation, because the swirling flow is much stronger in DT. The steady state computation by RANS does not contain the unsteady loss generated by the swirling flow. Therefore, the unsteady computation of DT is needed in the following study.

Figure 6 shows the efficiency hill diagram of the model turbine based on experimental results. The swirling flow counter-rotates the runner in the region above the no swirl line and corotates the runner in the region below. The shape of the hill diagram is wide in the horizontal direction which indicates that this model turbine is not sensitive to the fluctuation of rotational speed. Moreover, figure 7 shows the loss distribution of each flow path components. The Casing and SV loss are smaller than other losses because they are mainly dominated by friction loss. The GV loss is almost the same even though the Q_{11} changes near the design point. The DT loss is small near the design point because the swirl of flow is weak. The RV loss is the most main loss of each operating point, especially near the design point.

We are aiming at the further improvement of performance in the design point of the model turbine. Therefore, we mainly consider the loss mechanism of GV and RV around the design point.

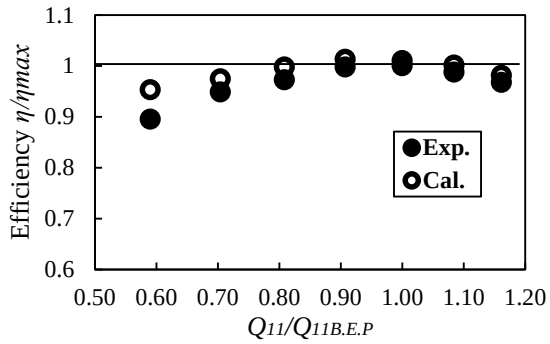

Figure 5. Efficiency at each operating point

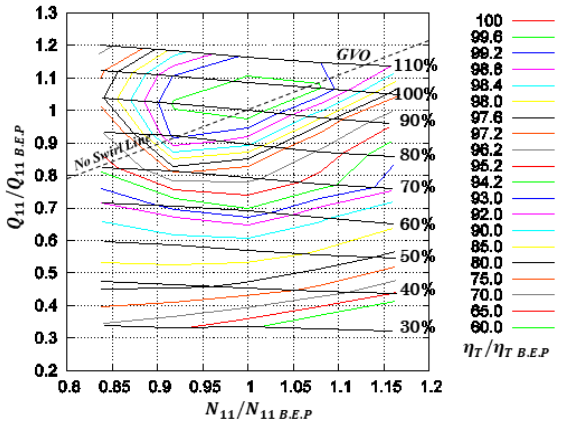

Figure 6. Efficiency hill diagram

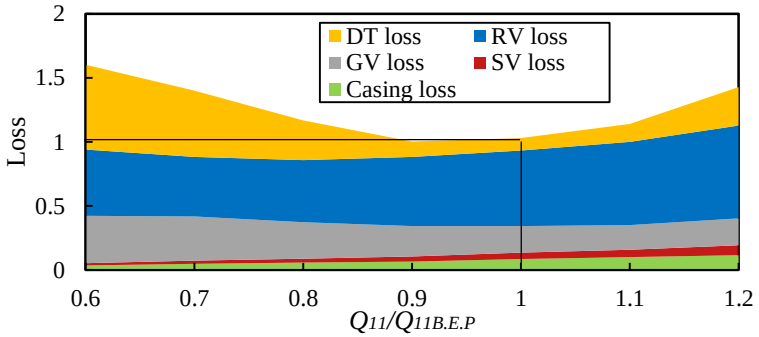

Figure 7. Loss distribution

5. Internal Flow and Loss Mechanisms

5.1. Double circular cascades

The static pressure distribution on the shroud side wall surface around GV and SV was measured in a double circular cascade. A comparison between the experimental results and the computational results is shown in figure 8. The results were arranged into SV and GV circumferential distribution, GV streamwise distribution and GV outlet circumferential distribution. The static pressure coefficient used is defined as

$$Cps = Ps(0.5\rho V_1^2)^{-1} \tag{4}$$

where V_1 is the absolute velocity at the inlet. The horizontal axis shows the angle from the beginning of the casing to show the position of measurement points.

Figure 8 shows that the experimental and computational results qualitatively agree with each other. However, a deviation between the experiment and the analysis result occurs near 120 degrees, at the GV outlet. The flow field is disturbed by the generation of vortex. Therefore, the isosurface of Q criterion around GV are used to visualize the vortex region in figure 9. Q criterion [8] is the second invariant of the velocity gradient tensor [9] which is defined as

$$Q = 0.5 \cdot (\|\bar{\Omega}\|^2 - \|\bar{S}\|^2) \tag{5}$$

where Ω is the vorticity tensor and S is the rate-of-strain tensor. The isosurface was coloured by the loss coefficient which is defined as

$$\zeta_{gv} = (Pt_{inlet} - Pt)(\rho g He)^{-1} \tag{6}$$

where Pt_{inlet} is the total pressure at the inlet. The vortex regions nearby the end wall and a horseshoe vortex region around the mid span were both confirmed between in the GV passage. Both regions extend from the GV inlet. Moreover, the vortex regions nearby the end wall coincide with the loss area, but the horseshoe vortex region does not. In addition, the isosurface coloured by swirling strength is shown in figure 10. The high swirling strength vortices and the loss region coincide, as can be observed on figure 9 and 10. The vortices could be thought as corner vortices. They are induced by the interference between the grown boundary layer near the end wall and the GV surface. However, the horseshoe vortex is considered as the inevitable vortex caused by the circulation around the GV. It is not the low energy fluid. Therefore, only the vortex regions nearby the end wall coincide with the loss area. The measurement point near 120 degrees is shown in figure 9 and 10 as a pink point which coincide with the vortex region. It might be the reason that the deviation between experimental and computational results occurs. The higher mesh resolution might be needed to estimate the effect on the static pressure of the measurement point from the vortex region more accurately. In conclusion, the main loss mechanism in the double circular cascade is the high swirling strength vortices extending from the GV inlet to the outlet near the end wall of GV.

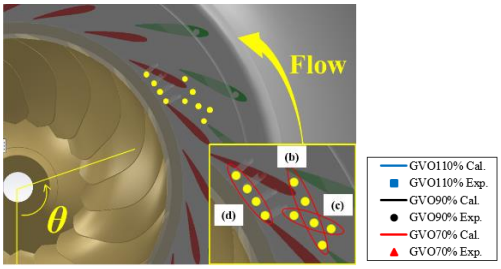

(a) Mesurement points location

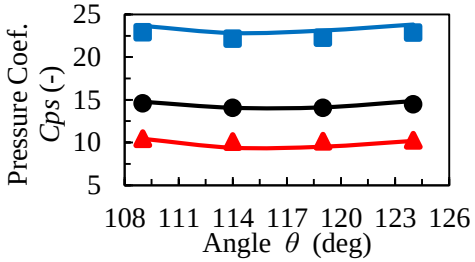

(b) SV and GV circumferential distribution

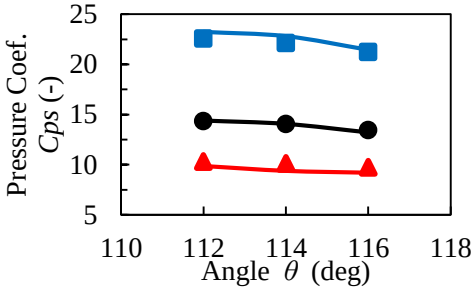

(c) GV streamwise distribution

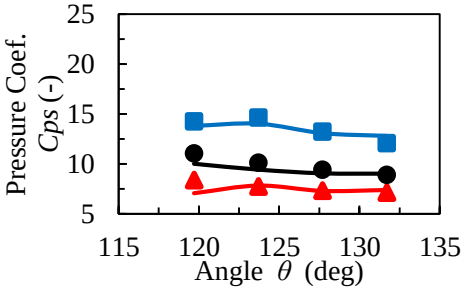

(d) GV outlet circumferential distribution

Figure 8. End wall static pressure distribution

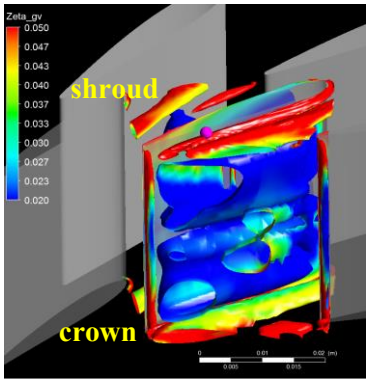

Figure 9. Isosurface of Q criterion coloured by the loss coefficient in GV

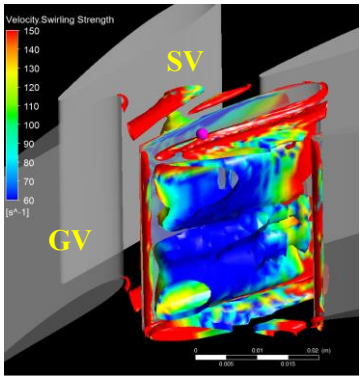

Figure 10. Isosurface of Q criterion coloured by swirling strength in GV

5.2. Shroudless runner

The steady static pressure distribution of the end wall on RV shroud side was measured. Figure 11 shows the position of measurement points. *Ls* represents the axial distance from the shroud inlet to the outlet of RV. *Lp* represents the distance from the inlet to the center of the measurement point. Figure 12 shows the comparison between experimental and computational results. Both results qualitatively agree with each other. Especially at the design points, at which they agree quantitatively. As a result, accurate predictions of the steady pressure field in RV at the design point is confirmed. Therefore, rothalpy and loss coefficient which are defined as

$$I = Ps \cdot \rho^{-1} + 0.5(W^2 - U^2) \tag{7}$$

$$\zeta_{rv} = (I_{ave@rv\_inlet} - I)U^{-2}{}_{ave@v\_inlet} \tag{8}$$

are used to evaluate the steady loss of RV. *W* represents the relative velocity and *U* is the rotational velocity.

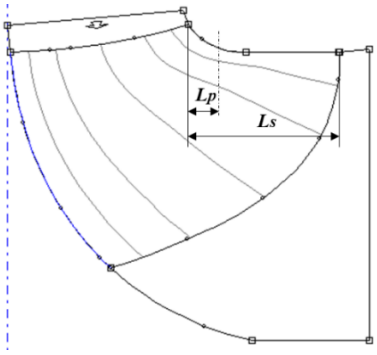

Figure 11. Definition of the measurement locations

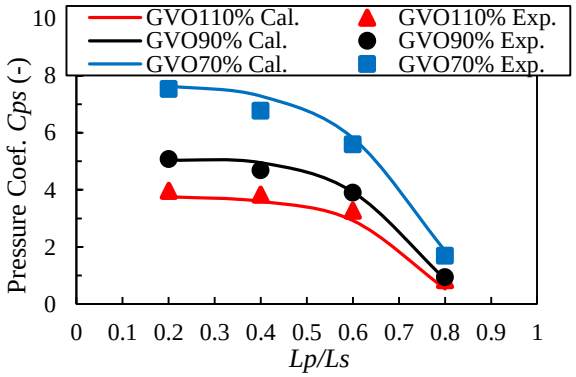

Figure 12. End wall static pressure distribution on the shroud side of RV

Figure 13 visualizes the vortex region of RV by Q criterion. It only shows the strongest region in which the helicity is larger than 25000 [m s^{-2}], conditions that imply a vortex swirling clockwise. A vortex is generated on the suction side of the blade in the shroud tip of RV can be confirmed extending from the inlet to the outlet. Further, the loss distribution between the blades and the vortex region overlap in figure 14. It is found that the vortex region coincides with the loss region, which imply that tip vortex occurance is one of the loss mechanisms of RV.

Figure 15 and 16 illustrate the loss distribution and the kinetic energy coefficient of the secondary flow which represents its intensity related to the main flow. The secondary vectors are also illustrated in these figures. The surfaces shown in figure 15 and 16 are aligned with the leading and trailing edges of the blades. The kinetic energy coefficient of the secondary flow is defined as

$$C_{KE} = V^2{}_{\sec} \cdot V^{-2}{}_{ave} \tag{9}$$

where V_{sec} represents the velocity of secondary flow and V_{ave} is the averaged bulk velocity on this surface.

Firstly, near the inlet of RV, the secondary flow is strong at the crown and shroud side, and near the pressure and the suction side. However, the loss is concentrated near the suction side and the shroud side. Near the suction side, it can be confirmed from secondary flow vectors that the secondary flow coming from the crown side collides with the suction surface and sharply deflects towards the shroud. Near the shroud, the leakage flow due to the tip clearance collides with the secondary flow. The leakage flow is diverted which implies that the secondary flow is stronger than the leakage flow. Both losses occur in places where the flow suddenly turns. Further, in the mid-cord, the leakage flow becomes stronger, and the secondary flow direction along the suction side is changed before it reaches the shroud. A part of the secondary flow collides with the leakage flow near the tip clearance and

sharply deflected. The loss region is also confirmed where the flow turns suddenly. Finally, the leakage flow becomes even stronger, and the leakage area like a jet is generated near the outlet of RV. The leakage region extends to the middle of the flow path which implies that the leakage flow is much stronger than the secondary flow. The secondary flow is steeply turned by the leakage flow and forms a large loss region.

According to the discussions above, a strong secondary flow does not directly generate the loss. The secondary flow collides with a wall or a leakage flow and the deflection will generate a loss region. The increasing deflected flow angle induces the loss in RV. In addition, we consider that the interference between the secondary flow and the leakage flow causes the tip leakage vortex.

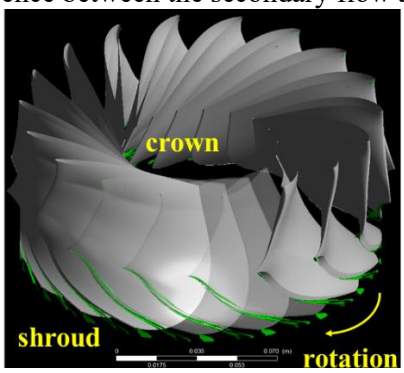

Figure 13. Q criterion of RV (Helicity > 25000 [m s^{-2}])

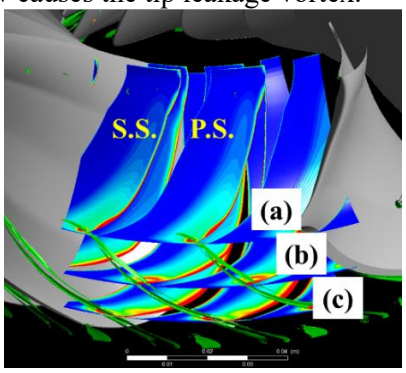

Figure 14. Q criterion and the loss distribution at cross sections in RV

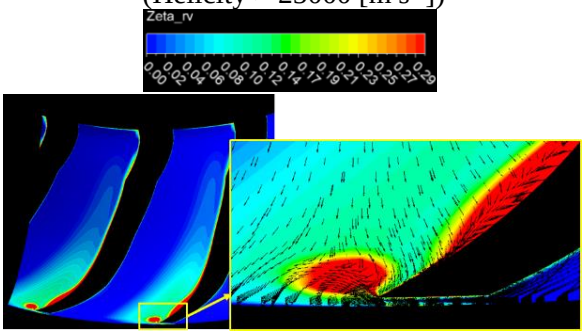

(a) near the inlet

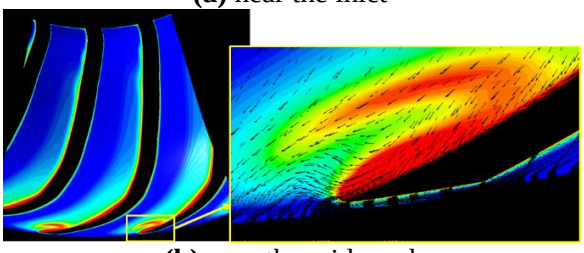

(b) near the mid-cord

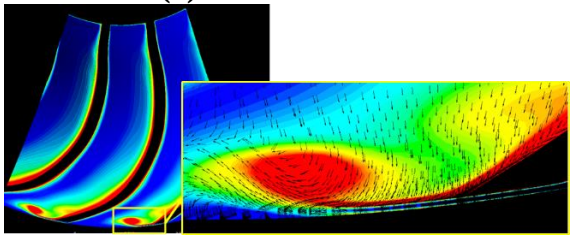

(c) near the outlet

Figure 15. Loss distribution and vectors of secondary flow in RV

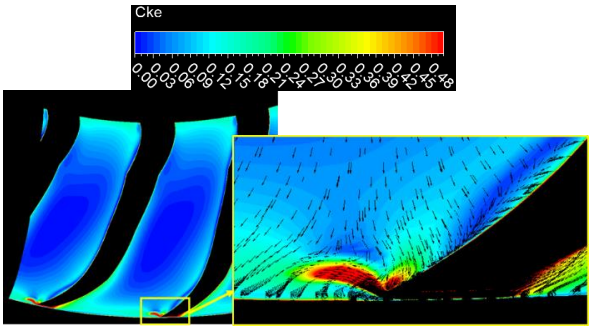

(a) near the inlet

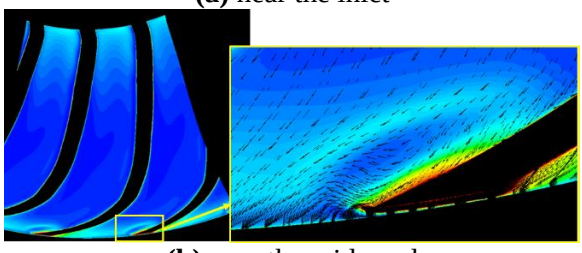

(b) near the mid-cord

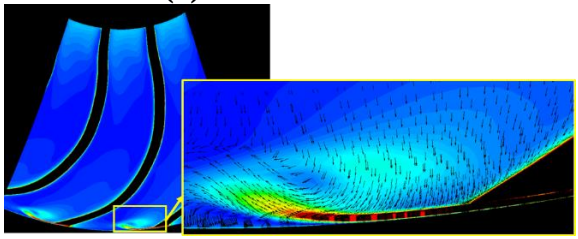

(c) near the outlet

Figure 16. Intensity of secondary flow and vectors of secondary flow in RV

5.3. Downstream of shroudless runner (in DT)

The velocity field and the pressure field of RV downstream were investigated by the three-hole pitot tube which enables time-averaged two-dimensional flow field analysis at each radial position. In figure 15, the total pressure, flow angle, radial distribution of axial velocity and tangential velocity results of experiments and computations were compared. $r0$ on the horizontal axis indicates the outer radius of the cross section of the pitot tube. Some dimensionless quantities are defined as

$$Cpt = Pt \cdot (0.5\rho V_1^{\,2})^{-1} \tag{10}$$

$$Vz^{*} = Vz \cdot Vm_{r2}^{\,-1} \tag{11}$$

$$Vt^{*} = Vt \cdot Vm_{r2}^{\,-1} \tag{12}$$

where the Pt, Vz, Vt, Vm_{r2} are the total pressure, axial velocity, tangential velocity and averaged bulk velocity at the outlet of RV respectively.

At the design point, the flow in the downstream of RV is almost non-swirling, which is confirmed by the qualitative agreement of the experimental and computational values. The steady state analysis by RANS predicts a stationary phenomenon in DT, which was confirmed. However, on the part load and the overload side, the trends of the experimental and computational results agree with each other, but the deviation of the values is large. The analysis overpredicts the axial and tangential velocity near the centre of DT ($r/r0 < 0.5$).

In addition, the part where the velocity sharply increases near the wall of the DT in the radial distribution of the axial velocity. It is thought that the tip leakage flow of the shroudless runner does not mix with the mainstream quickly downstream.

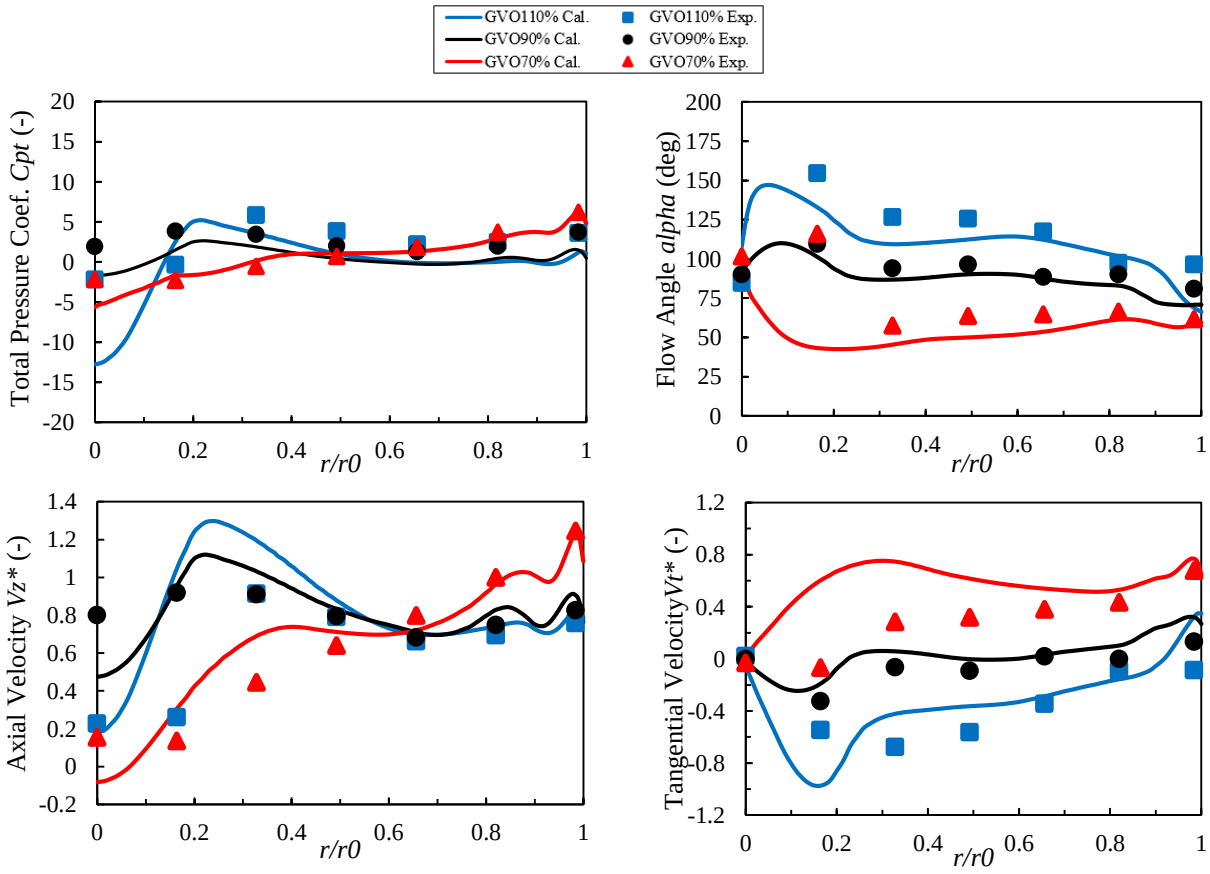

Figure 17. Radial distribution of pressure and velocity field

6. Conclusions

The accuracy of performance prediction, based on unitary stationary analysis using RANS, of the model turbine was confirmed by efficiency tests and internal flow measurements.

The loss in the shroudless runner is dominant.

The main loss mechanism of the double circular cascade occurs due to the high swirling strength vortices extending from the GV inlet to the outlet near the end wall of GV.

The strong secondary flow does not directly induce the loss. The secondary flow collides with a wall or a leakage flow and the deflection generates a loss region.

The main loss of the shroudless runner is due to the tip leakage vortex and the interference of the leakage flow and the secondary flow.

The tip leakage flow of the shroudless runner does not mix with the mainstream quickly at the downstream.

References

[1] Nakamura Y, Shima R, Komatsu H, Shiratori S and Miyagawa K (2015, July). Development of Shroudless Francis Turbine. In *ASME/JSME/KSME 2015 Joint Fluids Engineering Conference* (pp. V01AT02A006-V01AT02A006). American Society of Mechanical Engineers.

[2] Nakamura Y, Komatsu H, Shiratori S, Shima R, Saito S and Miyagawa K (2015, November). ICOPE-15-1164 Development of high-efficiency and low-cost shroudless turbine for small hydropower generation plant. In *The Proceedings of the International Conference on Power Engineering (ICOPE) 2015.12* (pp. _ICOPE-15). The Japan Society of Mechanical Engineers.

[3] Iino M, Tanaka K, Miyagawa K and Okubo T (2003). Numerical analysis of 3d internal flow with unstable phenomena in a centrifugal pump. In *Proceedings of the 7th Asian International Conference on Fluid Machinery*, Fukuoka, Japan, October (pp. 7-10).

[4] Iino M, Tanaka K, Miyagawa K and Okubo T (2003, July). Numerical simulation of hysteresis on head/discharge characteristics of a centrifugal pump. In *Proceedings of the ASME FEDSM 4th ASME_JSME Joint Fluids Engineering Conference*, Honolulu, HI, USA (pp. 6-10).

[5] Menter F R (1994). Two-equation eddy-viscosity turbulence models for engineering applications. *AIAA journal*, 32(8), 1598-1605.

[6] Braun O, Kueny J L and Avellan F (2005, June). Numerical analysis of flow phenomena related to the unstable energy-discharge characteristic of a pump-turbine in pump mode. In *None* (No. LMH-CONF-2009-005).

[7] Beaudoin M and Jasak H (2008, December). Development of a generalized grid interface for turbomachinery simulations with OpenFOAM. In *Open source CFD International conference* (Vol. 2). Berlin.

[8] ANSYS® Academic Research CFX. Release 17.2, Help System, CFD-Post User's Guide, ANSYS, Inc.

[9] Holmén V (2012). Methods for vortex identification. *Master's Theses in Mathematical Sciences*.